

A New Method for Reconstructing Magnetic Deflections from Sets of Proton Images

Joseph M. Levesque^{1, a)} and Lauren J. Beesley²

¹⁾*P-2, Fundamental and Applied Physics, Los Alamos National Laboratory, Los Alamos, New Mexico*

²⁾*A-1, Information Systems and Modeling, Los Alamos National Laboratory, Los Alamos, New Mexico*

(Dated: 21 June 2022)

Proton imaging is a powerful technique for imaging electromagnetic fields within an experimental volume, in which spatial variations in proton fluence are a result of deflections to proton trajectories due to interaction with the fields. When deflections are large, proton trajectories can overlap, and this nonlinearity creates regions of greatly increased proton fluence on the image, known as caustics. The formation of caustics has been a persistent barrier to reconstructing the underlying fields from proton images. We have developed a new method for reconstructing the path-integrated magnetic fields which begins to address the problem posed by caustics. Our method uses multiple proton images of the same object, each image at a different energy, to fill in the information gaps and provide some uniqueness when reconstructing caustic features. We use a differential evolution algorithm to iteratively estimate the underlying deflection function which accurately reproduces the observed proton fluence at multiple proton energies simultaneously. We test this reconstruction method using synthetic proton images generated for three different, cylindrically symmetric field geometries at various field amplitudes. The method we propose requires no assumption of deflection linearity and can reliably solve for fields underlying linear, nonlinear, and caustic proton image features for the selected geometries.

^{a)}Electronic mail: jmlevesq@umich.edu, jmlevesque@lanl.gov

I. INTRODUCTION

Reconstructing the underlying path-integrated magnetic fields from proton images is currently a topic of interest in magnetized high-energy-density (HED) experiments. In these experiments, deflections of the probe protons due to interaction with electromagnetic fields produce observable features in images of the proton fluence. The proton images only provide information of the final position of the protons at the image plane, and not their velocity. Reconstructing the deflection map or path-integrated field from a proton image is therefore nontrivial.

Multiple methods exist for reconstructing path-integrated magnetic fields from proton images in which the deflections are small and the proton image intensity is related to the deflections by a functional transformation.¹⁻⁴ Unfortunately, these methods tend to break down when the imparted deflections are such that neighboring proton trajectories intersect. When proton trajectories intersect, nonlinear increases in proton fluence known as caustics are observed on the image.⁵ The formation of caustics arises from sufficient combinations of field amplitude and field gradients, and is commonly observed in magnetized HED experiments.⁶⁻⁹ Because of the nonlinearity in proton positions on the image with respect to initial trajectory, when caustics are present there is no longer a functional transformation between proton image fluence and proton deflections.

Lacking a linear transformation between the proton image and deflections, it has so far been challenging, if not impossible, to accurately reconstruct from a proton image the path-integrated magnetic field which produce caustic features, though some attempts have been made to bridge this gap. For example, Kasim *et al.*¹⁰ used a computational geometry approach to reconstruction, succeeding with some test images in the weakly caustic regime, but failing when branching caustics appeared on the image. Chen *et al.*¹¹ trained a neural network to reconstruct a pseudo-3D magnetic field map from proton images for a limited set of field geometries, and also saw some success for some caustic test images, but failed in instances as a result of insufficient information from the provided proton image. Additionally, the performance of any neural network will depend heavily on its organization and the training set provided, which may reduce accuracy when presented with images of novel field configurations, which are likely to occur in experiment.

We propose a new reconstruction method to overcome some of the existing barriers of magnetic field reconstruction. The basis of our proposed method is that instead of reconstructing the deflections from a single proton image, we simultaneously reconstruct the magnetic deflections using multiple images of the same field, each image at a different proton energy. The additional

information provided by multiple images introduces some uniqueness in the reconstruction, because each image is ideally the result of the same path-integrated magnetic field. Our method of reconstructing deflections from a set of images, along with a realistic binning method to create the proton images, allows accurate reconstruction of deflections even in the caustic regime and further expands the regimes for which quantitative measurements of magnetic fields can be made via proton imaging.

In this paper we introduce a new method of reconstructing the underlying magnetic deflection field from sets of proton images of the same field structure at different proton energies. We use a differential evolution algorithm — a type of genetic optimization algorithm — to iteratively estimate the proton deflections as a function of initial proton trajectory and proton energy, searching for deflections which minimize a cost function based on the error between the synthetic reconstruction images and the data in addition to additional heuristic parameters. We restrict analysis and demonstration of this technique to cylindrically symmetric magnetic fields in which the proton deflection is solely in the radial direction so that we can consider pseudo-one dimensional proton intensity profiles. Section II outlines some basics of proton imaging and some issues when reconstructing underlying magnetic field deflections. Section III describes our differential evolution reconstruction method. Section IV displays results of this reconstruction method for three test cases: a Gaussian ellipsoid vector potential, a current-carrying wire segment, and a modified current-carrying wire segment with an additional Gaussian drop-off, each at three different field strengths. In Section V we discuss the benefits of this reconstruction method, with some insight on how it may be extended to reconstruction of arbitrary two-dimensional proton images. Section VI concludes the paper.

II. PROTON IMAGING

In this section we describe the process of proton imaging. The general proton imaging geometry is illustrated in Figure 1, in which the axis from the proton source to the object and image planes is z , L_O is the distance from the source to the center of the interaction region (the object plane), L_I is the distance from the proton source to the image plane, and L_{OI} is the distance from the object plane to the image plane. We limit our consideration to fields that are cylindrically symmetric and deflect protons in the radial direction. Proton deflections by magnetic fields in the interaction region are a function of the perpendicular magnetic field integrated along the proton's trajectory

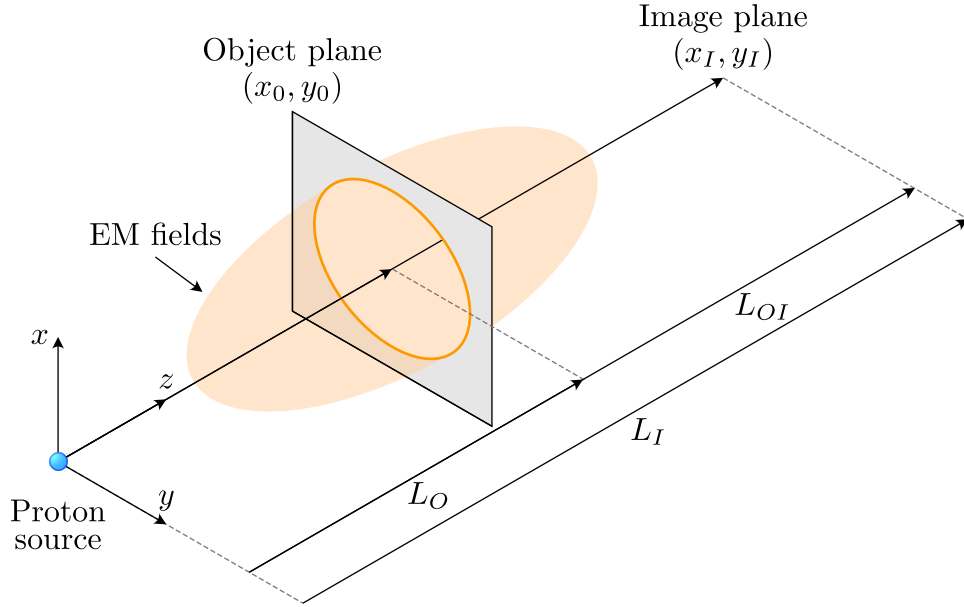


FIG. 1. Illustration of the general proton imaging geometry (not to scale). The protons are initialized from a point source and probe primarily along the z axis. The object plane is defined as the center of the interaction region, and the image plane is where the images are generated.

and the energy of the proton, as

$$\Delta\alpha = \frac{q}{\sqrt{2mE_p}} \int B_\phi dl, \quad (1)$$

where $\Delta\alpha$ is the deflection angle, q is the proton charge, m is the proton rest mass, E_p is the kinetic energy of the proton, B_ϕ is the magnetic field of interest, and l is the proton trajectory in the interaction region. For this paper we assume that the protons are emitted from a point source, so the protons naturally diverge with initial trajectories defined by the angles α_0 .

To simplify the imaging process, we assume that the deflections are only important over distances greater than the size of the interaction region, and that the trajectory of any proton remains constant within the interaction region. Using these assumptions, we calculate the deflection from the total path-integrated field along any ballistic trajectory and apply the deflection in a single step similarly to the approach of¹², backtracking to add the deflection at the object plane. The location at the image plane of any proton deflected by an amount $\Delta\alpha$ can then be calculated as

$$r_I = L_{OI} \tan(\alpha_0 + \Delta\alpha) + L_O \tan(\alpha_0) \quad (2)$$

where the first term is the deflected radial trajectory from the object plane to the image plane, and

the second term is the ballistic trajectory from the source to the object plane. When the fields are strong enough to significantly alter the proton trajectories within the interaction region, this method of adding path-integrated deflections in one breaks down and the protons must be integrated across the region in time, incurring additional computational cost.

When deflections are small and proton trajectories do not cross, it is sufficient to represent the image resulting from the deflected protons by a simple transformation depending on the Jacobian of the deflection in the image plane (x, y) , as

$$I = \frac{I_0 + \delta}{|\partial(x, y)/\partial(x_0, y_0)| + \delta} \quad (3)$$

where I is the proton fluence at the image, I_0 is the unperturbed proton fluence at the object plane, the coordinates x_0 and y_0 correspond to positions at the object plane, and δ is a small correction factor to limit the intensity.⁵ Existing field reconstruction methods are mostly limited to this small-deflection regime and reconstruct the field from single proton images by solving the Poisson equation or an optimal transport criterion.^{2,3} When protons are deflected in such a way that trajectories intersect one another, caustics appear on the image and the image transformation of equation (3) breaks down because the final location of protons on an image as a function of initial trajectory is no longer single-valued. When this transformation breaks down, existing methods of reconstruction also break down, though some reconstruction methods have proposed a possible extension of the transformation into the caustic regime.^{3,10}

In this paper we are concerned almost exclusively with the caustic regime, which requires that we fully consider the nonlinear proton trajectories. When generating synthetic proton images we account for the deflection of each proton, propagate them through the system, and bin them into discrete pixels at the image plane, mimicking the physical proton imaging procedure. Aside from the more complicated imaging process, the real difficulty in any reconstruction is that we only have a measure of the captured proton fluence and not proton velocity. The nonlinearity of proton trajectories introduced by caustics requires a nonlinear reconstruction approach.

III. RECONSTRUCTION METHOD

So how exactly can we hope to reconstruct deflection profiles which create caustic features if there is no single-valued mapping of intensity? We make use of an overlooked feature of most proton imaging experiments — multiple images of the same object at different proton energies.

Recall from equation (1) that for a given path-integrated magnetic field, protons are deflected proportionally to their energy as $E_p^{-1/2}$. Importantly, however, the location of image features does *not* share this proportionality. Therefore, by recognizing the lack of correlation between image features and deflections we can use multiple images of the same field to provide additional information and achieve some uniqueness when reconstructing the deflections.

We base our imaging on experiments at the OMEGA laser facility, which typically use the implosion of a D^3He capsule to produce a point-source of quasi-monoenergetic protons at 3 MeV and 14.7 MeV.^{13,14} We now redefine equation (1) to the more general form

$$\Delta\alpha(\alpha_0, E_p) = f(\alpha_0)/\sqrt{E_p}, \quad (4)$$

where the deflection for any proton trajectory α_0 is only a function of some value f and the proton energy. The goal of our reconstruction method is to find the underlying deflection field f which minimizes the error between synthetic, reconstructed images and the input images for the chosen proton energies simultaneously, in addition to minimizing extra heuristics.

In reconstructing the underlying deflection field of a caustic feature, we essentially need to determine the trajectory of each proton from its origin to the image to account for intersecting trajectories. Because of the large number of incident protons N_p in any image, solving for each proton trajectory individually — a continuous N_p -dimensional space — is computationally prohibitive. To more easily traverse the space of possible solutions, we assume a functional form for the deflection field as a function of initial proton trajectory α_0 . We define an estimated $f(\alpha_0)$ at a number n of nodes in space, where the nodes are fixed in α_0 position, and a continuous deflection function is generated by interpolating f between the node points. Using the continuous $f(\alpha_0)$ we can generate synthetic images for arbitrary initial proton distributions in α_0 . This method reduces the dimensionality of the parameter space to n dimensions, with n only on the order of 10, and greatly reduces computational cost. Even with a greatly reduced number of free parameters, there is still a large solution space to explore, so we need a method which allows us to quickly traverse the space to find a deflection function which best reproduces the images for our desired constraints.

We chose to solve this optimization problem using differential evolution, a type of genetic algorithm.^{15,16} Differential evolution (DE) is an iterative optimization method designed to handle tricky, non-convex problems. DE works by iteratively updating a population of solution candidates to find more optimal solutions based on the applied heuristic cost function. Each candidate c has its own genome, in this case a vector \mathbf{v}_c defining the deflections at each node n , where $\mathbf{v}_{c,n} = \Delta\alpha_{c,n}$.

For our problem, synthetic proton images at both energies are generated for each candidate, and each candidates is scored based on its error. We base our method on the canonical “DE/Rand/1” algorithm¹⁶, where for every iteration t the algorithm creates a new, offspring candidate vector \mathbf{u} by altering a number of randomly selected nodes via crossover determined by $rand(n) < CR$, where CR is the crossover rate, of a target candidate i based on the node values of two other randomly selected parent candidates j and k , as

$$\mathbf{u} = \mathbf{v}_i^{(t)} + F \times (\mathbf{v}_j^{(t)} - \mathbf{v}_k^{(t)}), \quad (5)$$

where F is the scaling parameter. CR and F are tuning parameters which affect the stiffness and rate of convergence of the population. If the deflection function of the offspring candidate produces images with a lower error than the original target candidate, the target candidate takes on the values of the mutant vector, $\mathbf{v}_i^{(t+1)} = \mathbf{u}$, and if the error is greater, the offspring candidate is rejected. The algorithm repeats until some stopping criteria for the error are met. By using a distributed population of potential candidates, DE is able to quickly explore a solution space and select more optimal solutions without getting stuck in local minima like a simpler gradient descent approach might.

Our differential evolution method is modified slightly from the “DE/Rand/1” algorithm in how the offspring vectors are generated, and in how they are accepted. During crossover the scaling factor F is changed to $F(1 + rand)$ to allow for additional variation in the potential search space. Additionally, even if the error of the offspring candidate is greater than the target candidate, it can still be accepted in our method. We occasionally allow the error to increase — if the error is within 25% of the original, there is a 20% chance that the offspring will be accepted, although a higher-error offspring will always be rejected if the target candidate is currently the lowest-error candidate in the population. This added chance of acceptance for the sub-optimal candidates in the population broadens the space available for mutations, and provides another way for the algorithm to escape from local minima.

The method for reconstructing the deflection function is as follows. First, we initialize the positions of the n nodes uniformly across the image. We then initialize the starting population with N_c number of candidates solutions with deflections functions f_c . To improve convergence, N_c is set to 100 for systems of dimensionality $n \lesssim 30$, and when $n > 30$, it is instead scaled to between $3N_c$ and $5N_c$ to have a sufficiently large population for convergence.¹⁷ Because we are only considering a one-dimensional radial deflection, each node only has one free parameter: a radial deflection

angle f_n . For each of the candidates, the deflection value f_n at each node is randomly initialized within a limited range. We limit the total range of deflections to between 0 and 0.5, and we find that further limiting this range during initialization to between 0 and 0.05 improves the rate of convergence. The reduced range during initialization allows the deflection field to build itself up in the early iterations, and usually prevents large variations between neighboring nodes that can compound and result in solutions with large oscillations. For each candidate we interpolate the f_n across the range of α_0 that reach the image using the Hermite interpolating polynomial method (PCHIP), which allows for curvature in the interpolant while maintaining the overall shape. We then generate the synthetic pseudo-1D proton image for each candidate, accounting for area changes. The synthetic images are normalized to maintain the same effective number of protons as in the data images. We then calculate the fitness of each candidate based on its synthetic images and deflection field using a number of heuristics.

When calculating the fitness of a candidate, the primary error heuristic we want to minimize is based on the difference of the reconstructed images to the input images. However, to further reduce the space of possible solutions and increase the accuracy of the solutions we also add extra heuristics to enforce some physical constraints. The total error of each candidate is calculated using three error heuristics and their associated weights as

$$\varepsilon_c^{(t)} = (w_1 \varepsilon_1^{(t)} + w_2 \varepsilon_2^{(t)})(1 + w_3 \varepsilon_3^{(t)}), \quad (6)$$

in which $\varepsilon_c^{(t)}$ is the error of candidate c at iteration t , and w_i is the scalar weight of error heuristic ε_i . The heuristics are calculated as follows:

$$\varepsilon_1 = \text{mean}(|I_{1,\text{recon}}(r)^2 - I_1(r)^2| / (I_1(r) + \delta)^2), \quad (7)$$

$$\varepsilon_2 = \text{mean}(|I_{2,\text{recon}}(r)^2 - I_2(r)^2| / (I_2(r) + \delta)^2), \quad (8)$$

$$\varepsilon_3 = \int_{\alpha_{0,\min}}^{\alpha_{0,\max}} \left[\frac{\sqrt{1 + (\alpha_1''(\alpha_0))^2}}{\alpha_{0,\max} - \alpha_{0,\min}} \right] \partial \alpha_0 - 1. \quad (9)$$

ε_1 and ε_2 are the primary error heuristics, and are the mean relative absolute square error between the candidate's reconstructed image and the actual image, where I_{recon} is the reconstruction candidate image, I is the data image, the subscripts 1 and 2 refer to the two proton energies, and $\delta = 0.01$ is a small correction factor to prevent the error from approaching infinity where the image intensity is zero. The summation of the image error at both energies ensures that the error of both (or all) images will be simultaneously minimized. Because the image error is the primary value we want

to minimize, the first image heuristic term on the left side of equation (6) is allowed to go to zero, ensuring that this will be the most important heuristic throughout the search. ϵ_3 is the difference of the arc length of the deflection gradient from the minimum length ($\alpha_{0,max} - \alpha_{0,min}$) as a ratio of this length. The heuristic $(1 + w_3\epsilon_3)$ enforces a level of smoothness in both the deflection field gradient and the deflection field by penalizing unnecessary oscillations in the deflection gradient. Limiting this secondary heuristic to a minimum value of 1 ensures that it will not dominate the reconstruction, particularly at later iterations.

For our tests, we use the following weights: $w_1 = 0.75$, $w_2 = 1$, and $w_3 = 10$. The increased weight on the high-energy proton image error can improve convergence, as the high-energy images are typically harder to fit. These weights can be tuned to be more or less constraining — reducing w_3 will reduce the smoothness constraint, for example. The differential evolution algorithm proceeds using $CR = 0.6$ and $F = 0.5$, until the error reaches a certain threshold, at which point the candidates are reinitialized with $2n - 1$ nodes, the starting values of which are obtained by pchip interpolation of the existing candidates. The higher-resolution reinitialization allows finer alteration of the deflection field to further minimize error, continuing with $CR = 0.2$. Despite increasing the resolution, initializing a larger number candidates is not necessary for convergence because the lower-resolution population has already converged significantly.

IV. RESULTS

In this section we test our reconstruction method on three cylindrically symmetric field configurations: a gaussian ellipsoid, a current-carrying wire, and a current-carrying wire with an additional exponential decrease. Each of our test cases are defined in a three-dimensional functional form. We calculate the total deflection field for each case by first integrating the magnetic field on a fine, regular grid within the range of initial trajectories that reach the image from the point source. The path-integrated magnetic field map is converted into a deflection map for both 3 MeV and 14.7 MeV proton energies, corresponding to energies from the D-³He capsule implosion source. The deflection maps are then interpolated to create higher-resolution maps as a function of initial proton trajectory. This functional form of the deflection map allows us to calculate deflections for arbitrary proton trajectories without having to perform integration for every proton trajectory.

To calculate the resulting images of these fields the protons are initialized as a point source

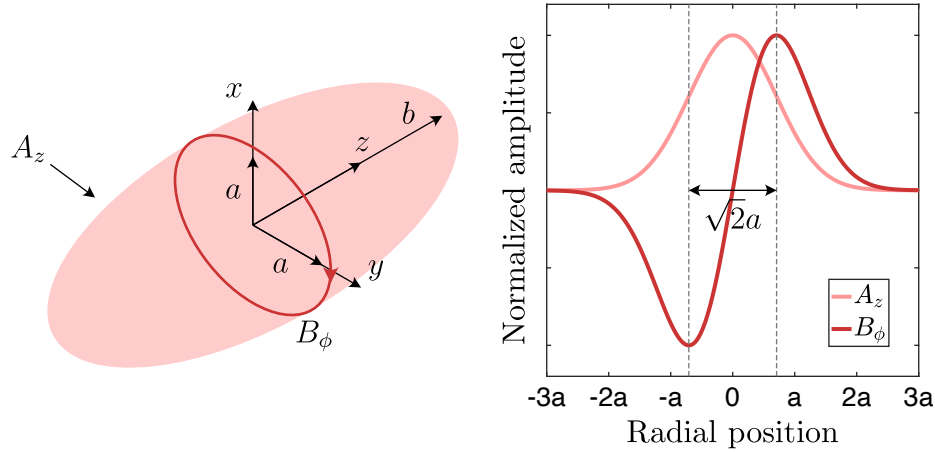


FIG. 2. An illustration of the gaussian ellipsoid vector potential and corresponding magnetic field alongside normalized plots of these quantities as a function of radius at the center plane. The primary proton probe trajectory is along z , the same axis as the vector potential component.

with fifty million protons in a uniform random distribution of α_0 that reach the image plane. The deflections are added at the center of the object plane L_O , and the protons travel with the new trajectories to the image plane at L_I to determine the final positions of the protons. The deflections are applied as in equation (2) and the two images are then created by binning the protons into discrete pixels in a 400x400 pixel image. To reduce the variation produced by randomness in the proton source initialization and to more closely resemble the fidelity of experimental CR39 images, we add a Gaussian blur of standard deviation 2 to the images. Because we are dealing with cylindrically symmetric deflections, we reduce each two-dimensional image into an averaged radial proton intensity 200 pixels in length. We use the one-dimensional proton fluence profiles as input to the reconstruction algorithm.

A. A Gaussian ellipsoid vector potential

Our first test case is the magnetic field defined by a single-component, Gaussian ellipsoidal vector potential. The vector potential is defined as in⁵,

$$A_z(x, y, z) = A_0 \exp \left[-\frac{(x-x_c)^2}{a^2} - \frac{(y-y_c)^2}{a^2} - \frac{(z-z_c)^2}{b^2} \right], \quad (10)$$

where A_0 is a constant that determines the amplitude of the vector potential, (x_c, y_c, z_c) denotes the center of the ellipsoid, a determines the effective radius of the ellipsoid perpendicular to the

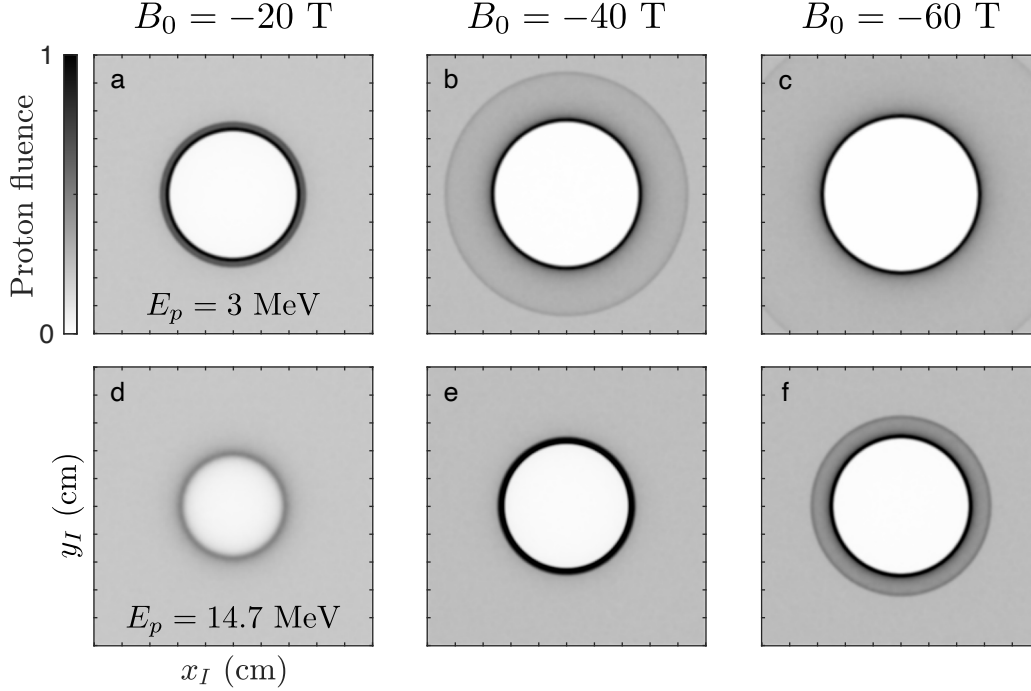


FIG. 3. Synthetic test proton images from the simulated Gaussian ellipsoid vector potential field as described by equation 10, using $a = 750 \mu\text{m}$, $b = 2 \text{ mm}$, at the magnetic field amplitudes $B_0 = -20 \text{ T}$, -40 T , and -60 T . (a,b,c) Synthetic 3 MeV proton images. (d,e,f) Synthetic 14.7 MeV proton images. The proton images are scaled by the maximum fluence at each field amplitude between both energy levels.

direction of the vector potential, and b is the effective size of the ellipsoid along the direction of the vector potential. For an ellipsoid centered at $x_c = y_c = 0$, $r = \sqrt{x^2 + y^2}$ and the magnetic field corresponding to this vector potential is

$$B_\phi(r, z) = B_0 \frac{r}{a} \exp \left[-\frac{r^2}{a^2} - \frac{(z - z_c)^2}{b^2} \right], \quad (11)$$

where B_0 is the magnetic field scaling factor which we use to define the field strengths. The relationship between the vector potential and the magnetic field is illustrated in Figure 2.

We only consider probing parallel to the axis of the vector potential, so the axis from the proton source to the image plane is z . Given the radial symmetry of the vector potential system and the orientation of A_z and B_ϕ with respect to the proton trajectories, the protons will be deflected radially inward when A_z and B_ϕ are positive, and radially outward when they are negative. For simplicity we further restrict the analysis to outward proton deflections, so the vector potential and magnetic field in the following examples are negative.

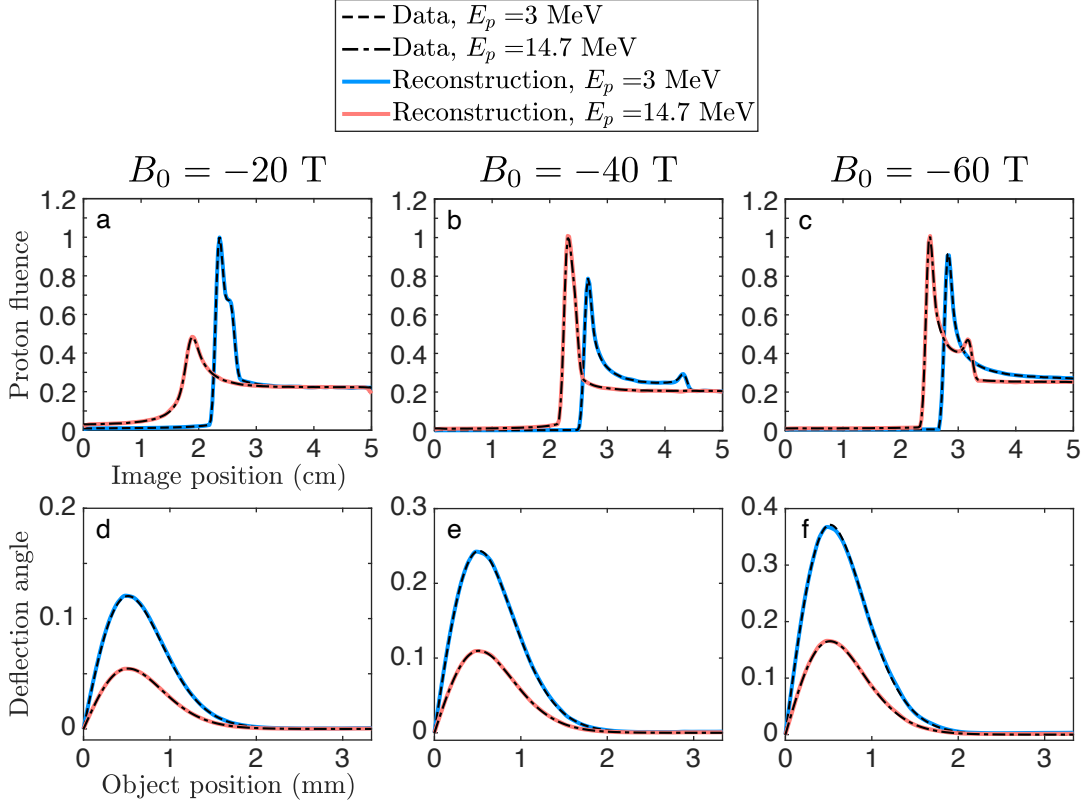


FIG. 4. Results of our reconstruction method on the synthetic images of Figure 3. (a,b,c) The known proton intensity (dashed lines) and reconstructed proton intensity profiles (solid lines). (d,e,f) The known radial deflection field (dashed lines) and reconstructed deflections (solid lines). Our proposed method accurately reconstructs both the underlying deflection and the proton fluence profiles simultaneously, even when some information is lost from the image at $B_0 = -60$ T.

Figure 3 shows synthetic test images at 3 MeV and 14.7 MeV proton energies for the Gaussian ellipsoid system defined by $a = 750 \mu\text{m}$, $b = 2$ mm, at the magnetic field amplitudes $B_0 = -20$ T, -40 T, and -60 T. This range of field amplitudes demonstrates the increasing prevalence of caustics as deflections increase. At -20 T, the 3 MeV image is in a weakly caustic regime, forming a void of protons in the center bounded by a branched, high-fluence ring; the 14.7 MeV image shows much less pronounced features and is in the linear deflection regime. As the field increases to -40 T the features are much more distinct — the secondary peak of the low-energy image has greatly expanding in radius, and the high-energy image is entering the caustic regime. At -60 T the protons which form the second peak in the low-energy image fall mostly outside of the image; the high-energy image is clearly caustic. We use averaged radial lineouts from both images at each

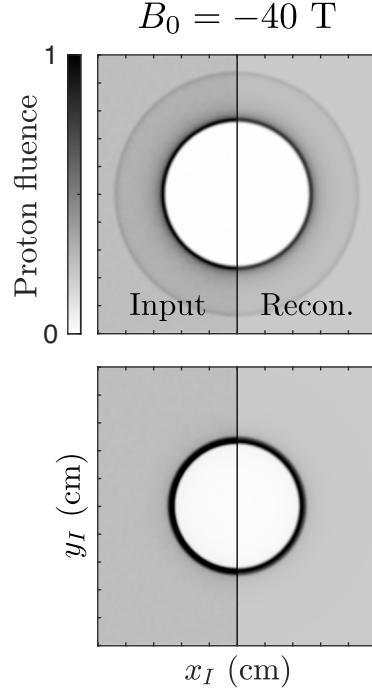


FIG. 5. Comparison of (left) the input images and (right) reconstructed images extrapolated from the 1D reconstruction of Figure 4 for the -40 T field ellipsoid at (top) 3 MeV and (bottom) 14.7 MeV proton energies.

field amplitude as input to our reconstruction algorithm.

Figures 4a-c show the synthetic proton fluence profiles and the corresponding reconstructed proton intensity profiles, and figures 4d-f show the actual deflection field alongside the reconstruction. We initialized the reconstruction with $n = 21$ nodes to start and increase to $n = 41$ after reaching $\epsilon_1 + \epsilon_2 < 0.05$, after which the computation proceeds for at most 350,000 iterations or until $\epsilon_1 + \epsilon_2 < 0.01$. Our reconstruction method very accurately reconstructs both the proton fluence profiles for both energies and the underlying deflection function. The error in the reconstructed proton fluence is almost negligible, less than a sum total 4% error across both images combined. Figure 5 compares the 2D test image with a 2D image extrapolated from the reconstructed 1D proton fluence profile at -40 T, further demonstrating that there is little difference between the two. For the Gaussian ellipsoid system the reconstruction method works equally well regardless of if the images are in the linear or caustic regimes, and is capable of reconstructing the deflections even when some information has been lost in the low-energy image at $B_0 = -60 \text{ T}$.

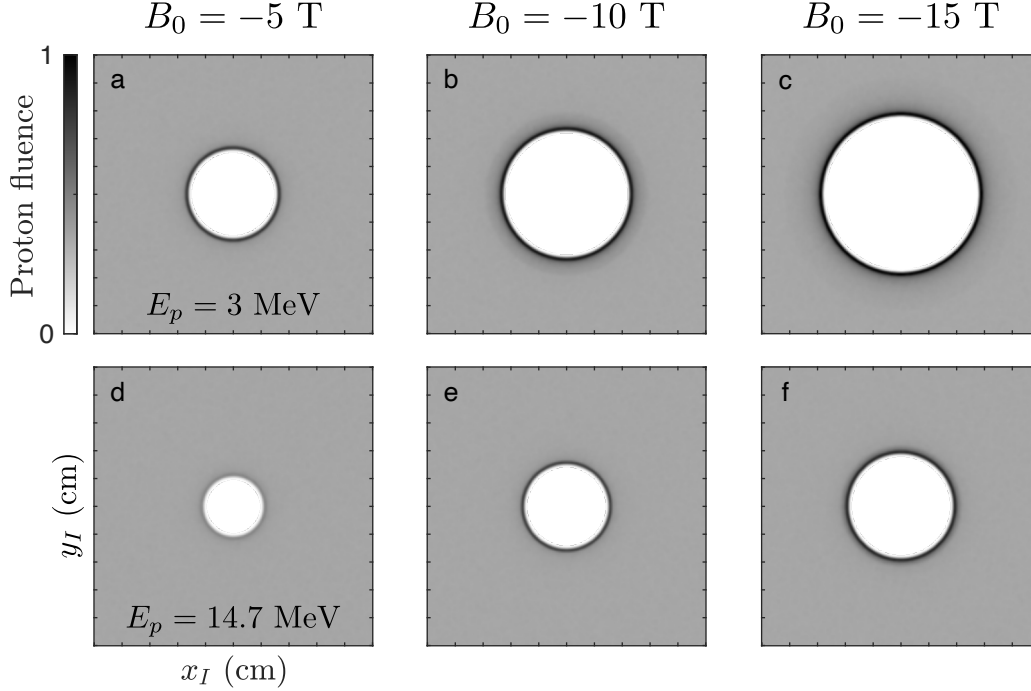


FIG. 6. Synthetic proton images from a simulated wire field as described by equation 12, with $R = 380$ μm at the magnetic field amplitudes $B_0 = -5$ T, -10 T, and -15 T. (a,b,c) Synthetic 3 MeV proton images. (d,e,f) Synthetic 14.7 MeV proton images. The sharp gradient of the field produces only a single caustic peak on each image.

B. A current-carrying wire

Next we consider the proton images produced by the magnetic field around a straight current-carrying wire segment. The field outside the wire is defined by

$$B_\phi(r) = B_0 \frac{R}{r}, \quad (12)$$

where R is the inner radius of the solid wire, and r is the distance from the center of the wire. The magnetic field is again in ϕ , so proton deflections are radially outward. Figure 6 shows the synthetic proton images for magnetic deflection from a 4 mm long segment of wire with $R = 380$ μm , at $B_0 = -5$ T, -10 T, and -15 T. Proton images of the $1/r$ field profile configuration are inherently caustic at any significant field strength, and the resulting sharp intensity profiles make this a challenging field to reconstruct.

The results of our reconstruction for the wire field are shown in Figure 7. We initialize the reconstruction in the same way as for the Gaussian ellipsoid field, using the same number of nodes

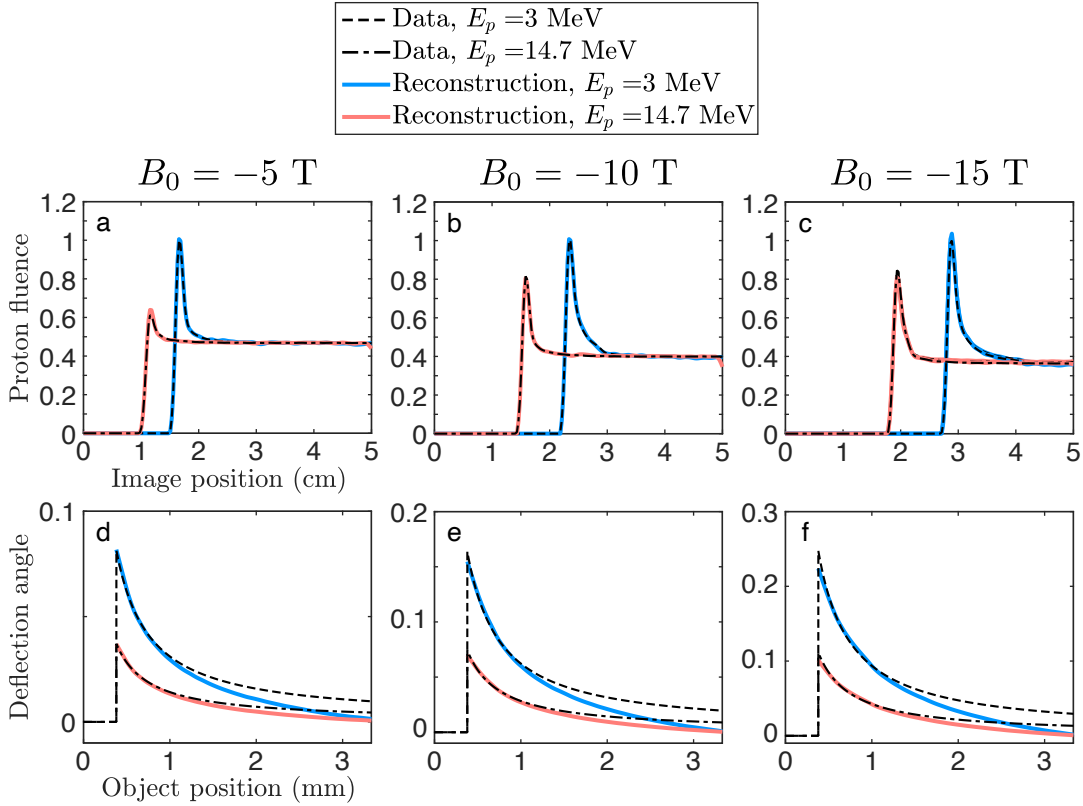


FIG. 7. Results from our reconstruction method on the images produced by Figure 6. (a,b,c) The known proton intensity (dashed lines) and reconstructed proton intensity profiles (solid lines). (d,e,f) The known radial deflection field (dashed lines) and reconstructed deflections (solid lines). The proton fluence profiles are reconstructed well, but the deflection reconstruction deviates significantly after 1 mm.

and the same stopping criteria. The reconstructed proton fluence profiles again match the input very well, but the deflection field has significant deviations. The reconstructed deflection fields match the actual deflection well for the first 1 mm of the object region, but decrease to zero much faster than the expected $1/r$. The poor agreement between reconstructed and actual deflection here is likely because the images have single, sharp peaks followed by smooth, almost uniform fluence. These results suggest that in these cases there is only significant information to reconstruct the main driver of the caustic, while the rest of the image can be the result of much lower deflection, which is preferred by our chosen heuristics.

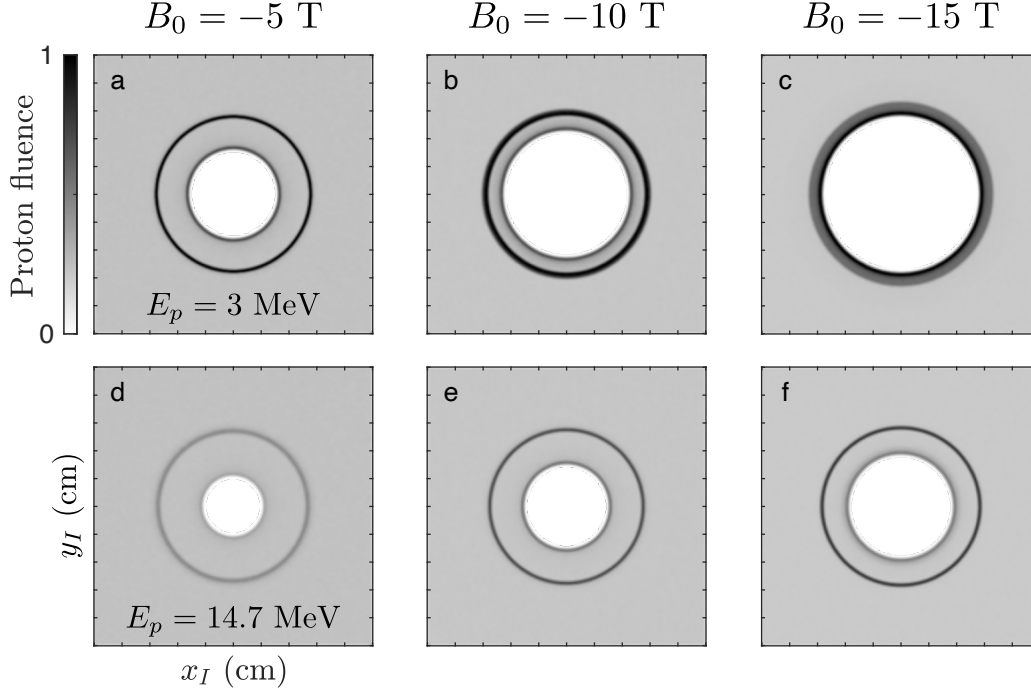


FIG. 8. Synthetic test proton images from a simulated current-carrying wire field with an additional Gaussian decrease as described by equation 13. (a,b,c) Synthetic 3 MeV proton images. (d,e,f) Synthetic 14.7 MeV proton images. Additional peaks are present because of the dropoff at a relatively fixed position regardless of field amplitude.

C. A current-carrying wire with an exponential decrease

Building on the previous section, we again set the base magnetic field from a current-carrying wire, but add a Gaussian decrease to zero with radius starting halfway across the object region, as

$$B_\phi(r) = B_0 \frac{R}{r} \exp \left[- \left(\frac{r - 1.62}{0.161} \right) \right], \quad (13)$$

where the units of r are again in mm. Physically, this situation could correspond to the presence of a conducting medium (like a plasma) impinging on the wire field, but still allowing the transmission of protons with minimal scattering to produce an image. The resulting proton images, shown in Figure 8, have additional features when compared to nominal wire field, which are strongly related to the curvature of the decrease. The Gaussian decrease causes the deflection from the wire to suddenly stop, and creates another pileup of protons on the image — a second caustic surface — corresponding roughly to the position at which the decrease occurs.

The reconstruction results of Figure 9 show much better agreement than the nominal wire field

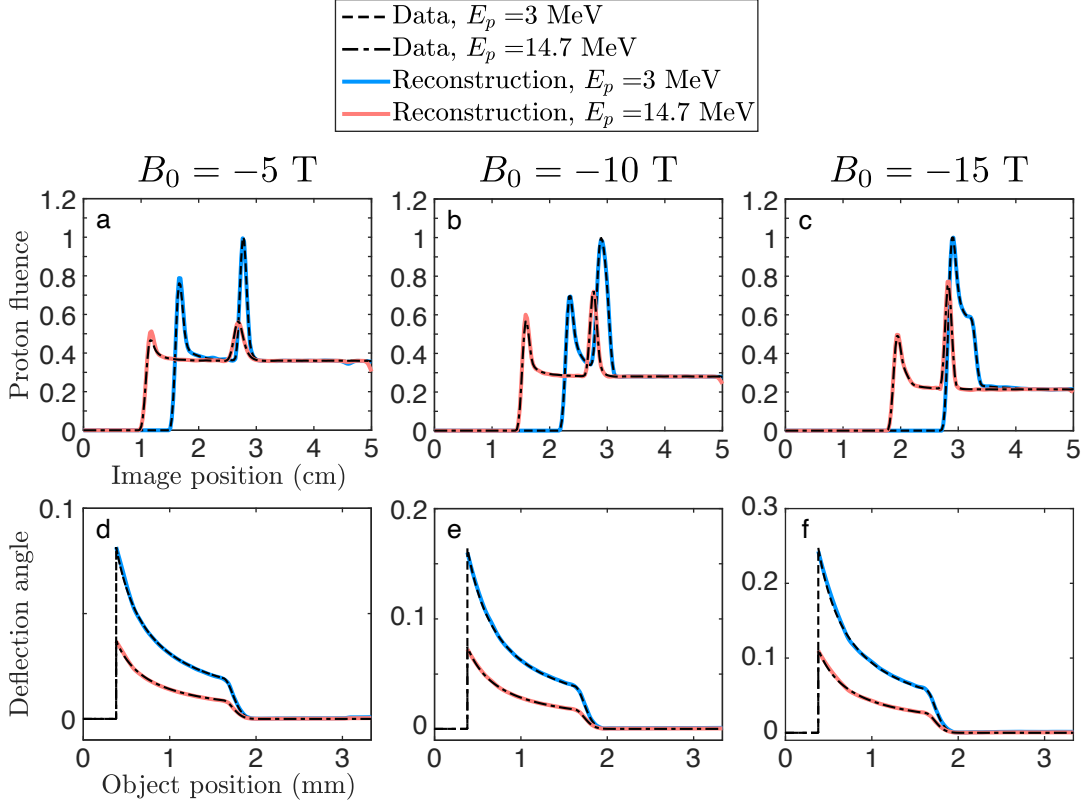


FIG. 9. Results from the deflection reconstruction method on the images produced by Figure 8. (a,b,c) The known proton intensity (dashed lines) and reconstructed proton intensity profiles (solid lines). (d,e,f) The known radial deflection field (dashed lines) and reconstructed deflections (solid lines). With the additional information from the Gaussian reduction, our reconstruction method finds the underlying deflections almost exactly, in contrast to the wire-only field.

case in both the proton fluence and deflection field with the input. In fact, the deflection function is now consistently reconstructed almost exactly, not only is the Gaussian decrease recovered, but the preceding $1/r$ profile matches better than for the nominal wire field. The increased fidelity is owed to the additional information from the second caustic on the image, which provides additional constraints on the deflection field.

V. DISCUSSION

Using two simultaneous proton images at different proton energies, our differential evolution algorithm can accurately reconstruct synthetic, symmetric deflection field profiles regardless of

if caustics are present on the images, with the exception of the wire-only field. We find that, at least in these cylindrically symmetric test cases, additional features in the proton image result in a better fit, likely because there is less degeneracy in the possible solution space. In terms of computational cost, for these test cases our method generally converges by 400,000 iterations and usually takes less than 20 minutes running the reconstruction as a MATLAB script on a single 3.8 GHz processor. There may be ways to further improve the convergence, particularly when increasing the resolution of the reconstruction, perhaps in the form of additional or alternative heuristics to optimize. One possibility may be the inclusion of a probabilistic method which uses DE to minimize the log-likelihood of the deflection with respect to the input images. Likelihood-based inference is attractive because it could also provide confidence intervals for the estimated deflection function.

The requirement of multiple images is not a significant barrier to many experimental application, because obtaining multiple, simultaneous images of a system is common in HED experiments. As discussed earlier, experiments at the OMEGA laser facility using the D^3He capsule implosion generate protons at 3 MeV and 14.7 MeV.^{13,14} Experiments using a capsule-implosion proton source typically evolve slowly compared to the duration of the source, producing two images of the same field structure at two very distinct proton energies. Alternatively, the target-normal sheath acceleration (TNSA) method of proton source production generates a large band of high-energy protons, and the resulting energies are discriminated by being captured at successive film slices to produce many images in a single shot.¹⁸ Many experiments which use TNSA have so far focused on its ability to capture very fast field evolution, rather than mostly static objects.^{4,19} However, the additional information available from a potentially large set of images could enable more complex and accurate reconstruction than with two images from the capsule implosion source.

Although we have restricted this paper to only consider pseudo-one-dimensional, cylindrically symmetric deflection fields, it is important to consider possible extension to two-dimensional deflection fields. The underlying method of using multiple images should also be valid for reconstructing the full path-integrated field, but in terms of the differential evolution algorithm a number of complications need to be addressed. First, the addition of a second dimension necessitates an increase in the number of nodes needed to sufficiently define the deflection field, with a corresponding increase in the computational cost. Second, if allowing for nonuniform, asymmetric images the choice of node position will also be important for caustic reconstruction, although a

sufficiently fine grid could avoid this issue at a cost. Third — and probably most importantly — the underlying deflection function will require at minimum two values: the deflection amount and the deflection direction. The two-component deflection solution space should be more efficient than considering a full three-component field. It is not obvious as to whether both quantities will need to be evolved simultaneously, or in an alternating manner. It is also not yet clear if two images would be enough to adequately constrain both the direction and the amount of deflection for reconstruction — additional proton images may be required.

VI. CONCLUSION

In conclusion, we have developed a new method for reconstructing underlying path-integrated magnetic deflections from a set of two proton images of the same object, each at a different proton energy. We use a differential evolution algorithm to iteratively evolve an underlying deflection function to simultaneously reconstruct the proton fluence profiles on the two input images. The differential optimization scheme requires few assumptions in reconstruction, where most information comes from the presence of multiple images. Our method is able to accurately reconstruct the deflections regardless of nonlinearities (caustics) in the proton image, as long as the images provide sufficient information. This is among the first reconstruction method truly able to deal with caustics, albeit in a limited geometry, and equally applicable to non-caustic features. Further improvements should enable expansion to arbitrary 2D geometries, and the differential evolution optimization could enable transition to and improvements in neural-network-based reconstruction.

DATA AVAILABILITY

We will make the MATLAB scripts developed in this work openly available for general use.

ACKNOWLEDGEMENTS

This work was partially funded by the U.S. Department of Energy, through the NNSA Center of Excellence under cooperative agreement number DE-NA0003869, the NNSA-DP and SC-OFES Joint Program in HEDLP, grant number DE-NA0002956, the NLUF Program and Rice University, grant numbers DE-NA0002722 and DE-NA0002719. This work was also supported by the U.S. Department of Energy through the Los Alamos National Laboratory. Los Alamos National

Laboratory is operated by Triad National Security, LLC, for the National Nuclear Security Administration of U.S. Department of Energy (Contract No. 89233218CNA000001).

REFERENCES

- ¹M. C. Levy, D. D. Ryutov, S. C. Wilks, J. S. Ross, C. M. Huntington, F. Fiuza, D. A. Martinez, N. L. Kugland, M. G. Baring, and H.-S. Park, *Review of Scientific Instruments* **86**, 033302 (2015), <https://doi.org/10.1063/1.4909536>.
- ²C. Graziani, P. Tzeferacos, D. Q. Lamb, and C. Li, *Review of Scientific Instruments* **88**, 123507 (2017), <https://doi.org/10.1063/1.5013029>.
- ³A. F. A. Bott, C. Graziani, P. Tzeferacos, T. G. White, D. Q. Lamb, G. Gregori, and A. A. Schekochihin, *Journal of Plasma Physics* **83**, 905830614 (2017).
- ⁴C. A. J. Palmer, P. T. Campbell, Y. Ma, L. Antonelli, A. F. A. Bott, G. Gregori, J. Halliday, Y. Katzir, P. Kordell, K. Krushelnick, S. V. Lebedev, E. Montgomery, M. Notley, D. C. Carroll, C. P. Ridgers, A. A. Schekochihin, M. J. V. Streeter, A. G. R. Thomas, E. R. Tubman, N. Woolsey, and L. Willingale, *Physics of Plasmas* **26**, 083109 (2019), <https://doi.org/10.1063/1.5092733>.
- ⁵N. L. Kugland, D. D. Ryutov, C. Plechaty, J. S. Ross, and H.-S. Park, *Review of Scientific Instruments* **83**, 101301 (2012), [10.1063/1.4750234](https://doi.org/10.1063/1.4750234).
- ⁶N. L. Kugland, D. D. Ryutov, P.-Y. Chang, R. P. Drake, G. Fiksel, D. H. Froula, S. H. Glenzer, G. Gregori, M. Grosskopf, M. Koenig, Y. Kuramitsu, C. Kuranz, M. C. Levy, E. Liang, J. Meinecke, F. Miniati, T. Morita, A. Pelka, C. Plechaty, R. Presura, A. Ravasio, B. A. Remington, B. Reville, J. S. Ross, Y. Sakawa, A. Spitkovsky, H. Takabe, and H.-S. Park, *Nature Physics* **8**, 809 EP (2012).
- ⁷N. L. Kugland, J. S. Ross, P.-Y. Chang, R. P. Drake, G. Fiksel, D. H. Froula, S. H. Glenzer, G. Gregori, M. Grosskopf, C. Huntington, M. Koenig, Y. Kuramitsu, C. Kuranz, M. C. Levy, E. Liang, D. Martinez, J. Meinecke, F. Miniati, T. Morita, A. Pelka, C. Plechaty, R. Presura, A. Ravasio, B. A. Remington, B. Reville, D. D. Ryutov, Y. Sakawa, A. Spitkovsky, H. Takabe, and H.-S. Park, *Physics of Plasmas* **20**, 056313 (2013), <https://doi.org/10.1063/1.4804548>.
- ⁸C. M. Huntington, F. Fiuza, J. S. Ross, A. B. Zylstra, R. P. Drake, D. H. Froula, G. Gregori, N. L. Kugland, C. C. Kuranz, M. C. Levy, C. K. Li, J. Meinecke, T. Morita, R. Petrasso, C. Plechaty, B. A. Remington, D. D. Ryutov, Y. Sakawa, A. Spitkovsky, H. Takabe, and H. S. Park, *Nature*

- Physics **11**, 173 (2015).
- ⁹C. M. Huntington, M. J.-E. Manuel, J. S. Ross, S. C. Wilks, F. Fiuza, H. G. Rinderknecht, H.-S. Park, G. Gregori, D. P. Higginson, J. Park, B. B. Pollock, B. A. Remington, D. D. Ryutov, C. Ruyer, Y. Sakawa, H. Sio, A. Spitkovsky, G. F. Swadling, H. Takabe, and A. B. Zylstra, *Physics of Plasmas* **24**, 041410 (2017), <https://doi.org/10.1063/1.4982044>.
- ¹⁰M. F. Kasim, L. Ceurvorst, N. Ratan, J. Sadler, N. Chen, A. Sävert, R. Trines, R. Bingham, P. N. Burrows, M. C. Kaluza, and P. Norreys, *Phys. Rev. E* **95**, 023306 (2017).
- ¹¹N. F. Y. Chen, M. F. Kasim, L. Ceurvorst, N. Ratan, J. Sadler, M. C. Levy, R. Trines, R. Bingham, and P. Norreys, *Phys. Rev. E* **95**, 043305 (2017).
- ¹²J. Levesque, C. Kuranz, T. Handy, M. Manuel, and F. Fiuza, *Physics of Plasmas* **26**, 102303 (2019), <https://doi.org/10.1063/1.5100728>.
- ¹³C. K. Li, F. H. Séguin, J. A. Frenje, J. R. Rygg, R. D. Petrasso, R. P. J. Town, P. A. Amendt, S. P. Hatchett, O. L. Landen, A. J. Mackinnon, P. K. Patel, V. A. Smalyuk, J. P. Knauer, T. C. Sangster, and C. Stoeckl, *Review of Scientific Instruments* **77**, 10E725 (2006).
- ¹⁴C. K. Li, F. H. Séguin, J. A. Frenje, M. Manuel, D. Casey, N. Sinenian, R. D. Petrasso, P. A. Amendt, O. L. Landen, J. R. Rygg, R. P. J. Town, R. Betti, J. Delettrez, J. P. Knauer, F. Marshall, D. D. Meyerhofer, T. C. Sangster, D. Shvarts, V. A. Smalyuk, J. M. Soures, C. A. Back, J. D. Kilkenny, and A. Nikroo, *Physics of Plasmas* **16**, 056304 (2009), <https://doi.org/10.1063/1.3096781>.
- ¹⁵R. Storn and K. Price, *Journal of Global Optimization* **11**, 341 (1997).
- ¹⁶S. Das, S. S. Mullick, and P. Suganthan, *Swarm and Evolutionary Computation* **27**, 1 (2016).
- ¹⁷A. P. Piotrowski, *Swarm and Evolutionary Computation* **32**, 1 (2017).
- ¹⁸S. P. Hatchett, C. G. Brown, T. E. Cowan, E. A. Henry, J. S. Johnson, M. H. Key, J. A. Koch, A. B. Langdon, B. F. Lasinski, R. W. Lee, A. J. Mackinnon, D. M. Pennington, M. D. Perry, T. W. Phillips, M. Roth, T. C. Sangster, M. S. Singh, R. A. Snavely, M. A. Stoyer, S. C. Wilks, and K. Yasuike, *Physics of Plasmas* **7**, 2076 (2000), <https://doi.org/10.1063/1.874030>.
- ¹⁹L. Gao, H. Ji, G. Fiksel, W. Fox, M. Evans, and N. Alfonso, *Physics of Plasmas* **23**, 043106 (2016), <https://doi.org/10.1063/1.4945643>.